# Modeling of passive microwave responses in convective situations using outputs from mesoscale models : comparison with TRMM/TMI satellite observations.

M. Wiedner, Christophe Prigent, J.-R. Pardo, O. Nuissier, Jean-Pierre Chaboureau, Jean-Pierre Pinty, P. Mascart

# Modeling of passive microwave responses in convective situations using output from mesoscale models: Comparison with TRMM/TMI satellite observations

Martina Wiedner,[1,2] Catherine Prigent,[1] Juan R. Pardo,[3] Olivier Nuissier,[4] Jean-Pierre Chaboureau,[4] Jean-Pierre Pinty,[4] and Patrick Mascart[4]

Received 24 October 2003; revised 27 January 2004; accepted 5 February 2004; published 30 March 2004.

[1] Passive microwave observations are sensitive to the whole hydrometeor column, in contrast to infrared and visible observations, which essentially sense cloud tops. Therefore passive microwave observations are a very promising tool to study the internal structure of precipitating clouds. A microwave radiative transfer model (Atmospheric Transmission at Microwaves (ATM)) has been developed to accurately simulate brightness temperature $T_B$ fields using output from nonhydrostatic mesoscale atmospheric model, Meso-NH, simulations. The radiative transfer code takes the detailed description of the hydrometeor properties (as simulated by the Meso-NH model) into account. The sensitivity of the predicted brightness temperature $T_B$ to the hydrometeor properties is carefully analyzed. Depending on the frequency, the passive microwave simulations show different sensitivities to the hydrometeor and surface properties: The low frequencies (10–30 GHz) sense essentially the surface properties and the liquid water column, whereas the higher frequencies (30–90 GHz) are most sensitive to the large icy hydrometeors (graupel and snow). $T_B$ simulations are generated for two real convective situations studied with Meso-NH: Hurricane Bret on 22–23 August 1999 in the Gulf of Mexico and a South Atlantic Convergence Zone case off the Brazilian coast on 6–7 February 2001. The radiative transfer simulations are compared to the corresponding Tropical Rainfall Measuring Mission (TRMM) Microwave Instrument (TMI) observations on board TRMM, at 10.65, 19.35, 22.24, 37, and 85.5 GHz. To our knowledge, no direct comparisons between simulated $T_B$ and satellite observations had been conducted before for a systematic evaluation of the mesoscale cloud models. An overall good agreement is obtained for both situations, especially for the second one. At high frequencies the agreement is particularly remarkable, given the high sensitivity of these frequencies to the particle characteristics, especially in the ice phase. This result gives us strong confidence not only in the radiative transfer model but also in the bulk microphysical scheme of Meso-NH. *INDEX TERMS:* 3314 Meteorology and Atmospheric Dynamics: Convective processes; 3329 Meteorology and Atmospheric Dynamics: Mesoscale meteorology; 3360 Meteorology and Atmospheric Dynamics: Remote sensing; *KEYWORDS:* radiative transfer modeling, mesoscale model, passive microwave

**Citation:** Wiedner, M., C. Prigent, J. R. Pardo, O. Nuissier, J.-P. Chaboureau, J.-P. Pinty, and P. Mascart (2004), Modeling of passive microwave responses in convective situations using output from mesoscale models: Comparison with TRMM/TMI satellite observations, *J. Geophys. Res.*, *109*, D06214, doi:10.1029/2003JD004280.

## 1. Introduction

[2] Mesoscale atmospheric models provide spatial and temporal predictions of heat and water transfer in the atmosphere as well as the distribution of hydrometeors in the vertical column. Using a microphysical parameterization of heat and water exchanges, the sources and sinks of several microphysical species (including cloud droplets, ice crystals, rain drops, snowflakes, and graupel) are calculated explicitly.

[3] Mesoscale models are usually evaluated by comparing their prediction with measurements of temperatures, wind speeds, precipitation etc., which are collected during large experiments such as Fronts and Atlantic Storm-Track Experiment (FASTEX) or Tropical Ocean Global Atmosphere–Coupled Ocean Atmosphere Response Experiment (TOGA-COARE). However, even during these well-documented campaigns, assessment of the highly variable cloud fields are barely possible, given the limited spatial and

[1]Laboratoire d'Étude du Rayonnement et de la Matière en Astrophysique, CNRS, Observatoire de Paris, Paris, France.
[2]I. Physikalisches Institut, Universität zu Köln, Cologne, Germany.
[3]Departamento de Astrofísica Molecular e Infrarroja, Instituto de Estructura de la Materia, Consejo Superior de Investigaciones Científicas, Madrid, Spain.
[4]Laboratoire d'Aérologie, Toulouse, France.


0148-0227/04/2003JD004280

temporal sampling of the in situ microphysical measurements. Model to satellite approaches have been suggested, in which simulated radiances using output from the atmospheric model are compared to satellite observed radiances. This method has already been successfully used to verify nonhydrostatic mesoscale atmospheric model, Meso-NH, predictions of water vapor and cloud tops by comparing them with the water vapor and thermal infrared channels of Meteosat [*Chaboureau et al.*, 2000, 2002].

[4] Passive microwave observations are sensitive to the whole hydrometeor column, in contrast to infrared observations that essentially only sense the cloud tops. Emission, absorption, and scattering depend strongly on the observed wavelength as well as on the hydrometeor characteristics. Depending on the observed wavelength and on the hydrometeor characteristics, microwave radiation is differently affected by emission, absorption, and scattering. Emission/absorption by liquid particles causes brightness temperatures to increase over a radiatively cold background such as the ocean. In contrast, scattering by larger, frozen hydrometeors reduces the amount of radiation measured by the satellite, especially at frequencies above 50 GHz.

[5] A model to satellite approach using passive microwave observations would be particularly suitable to evaluate the liquid and ice amounts generated by the cloud model. Analysis of the passive microwave radiative transfer sensitivity to cloud parameters have been performed using output from cloud models (e.g., by *Smith et al.* [1992] using the *Tripoli and Cotton* [1982] cloud model). *Kummerow and Giglio* [1994] and *Mugnai et al.* [1993] developed rain profile retrievals from satellite data based on $T_B$ simulations using output from cloud models. However, to our knowledge, no direct comparisons between simulated $T_B$ and satellite observations have been conducted for a systematic evaluation of the mesoscale cloud models. Comparisons of modeled cloud fields with cloud quantities retrieved from space-borne microwave sensors have already been performed. For instance, integrated cloud liquid water fields from the model can be compared to estimates from passive microwave satellite instruments [e.g., *Chaboureau et al.*, 2002]. However, it is often difficult to separate errors from the cloud model from those related to satellite retrieval. Each algorithm developed to extract an atmospheric parameter from satellite observations has its own assumptions. In the method we propose, simulated $T_B$ at several wavelengths will have to match all the corresponding observations, meaning that we will implicitly check the consistency of several atmospheric and surface quantities at the same time.

[6] The objectives of this study are as follows: (1) To develop a radiative transfer model that takes into account the detailed description of the hydrometeor column, as described by the mesoscale cloud model output. The Atmospheric Transmission at Microwaves (ATM) radiative transfer model [*Pardo et al.*, 2001; *Prigent et al.*, 2001] is adapted and used. (2) To compare the resulting $T_B$ output to passive microwave observations. The Tropical Rainfall Measuring Mission (TRMM) Microwave Instrument (TMI) on board the TRMM covers a large spectral domain (10–85 GHz) in both linear polarizations, with adequate spatial resolution. The TMI frequency channels are sensitive to the various particle types, from rain to ice particles. (3) To analyze potential discrepancies between simulated and observed $T_B$ using the experience of both the Meso-NH and the microwave radiative transfer groups. (4) To develop a tool that can be used "online" to evaluate the Meso-NH mesoscale model.

[7] In this paper, the Meso-NH atmospheric model is briefly described, with emphasis on the microphysical scheme (section 2). In section 3, the main features of the ATM microwave radiative transfer model related to this work are presented. Section 4 describes important changes to the microwave transfer code input concerning particle distribution and characterization, as well as an analysis of the sensitivity of $T_B$ to the particle properties. Simulated and observed brightness temperatures are compared in section 5 for two very different meteorological situations. Conclusions and perspectives are presented in the last section.

## 2. Meso-NH Atmospheric Model

[8] Meso-NH is a nonhydrostatic mesoscale model, jointly developed by Météo-France and the Centre National de la Recherche Scientifique (CNRS). Its general characteristics, as well as specific parameters chosen for this study, are summarized in Tables 1 and 2. A detailed description of the Meso-NH is given by *Lafore et al.* [1998] and the mixed-phase microphysical scheme developed by *Pinty and Jabouille* [1998] is described in the next subsection.

[9] Two numerical experiments are discussed in this study (Table 1). One experiment considers the structure of Hurricane Bret on 22–23 August 1999, while the other focuses on the South Atlantic Convergence Zone (SACZ) off the Brazilian coast on 6–7 February 2001. For both of them, temperature, wind, surface pressure, water vapor, and sea surface temperature taken from the European Centre for Medium-Range Weather Forecasts (ECMWF) 6-hourly analysis are used as initial and boundary conditions. In both cases, two-way grid-nesting simulations [*Stein et al.*, 2000] are used. The same parameterization is used for all the nested grids (Table 1), except for the convection parameterization which is not activated in the innermost grid (explicit cloud only). Results presented here are from the innermost grid only.

[10] Hurricane Bret has been simulated with four nested models, with a horizontal grid spacing of 55, 15, 5, and 1.67 km. The innermost grid covers 300 km × 300 km. The vertical grid has 44 levels with a grid spacing of 100 m close to the surface to 600 m at high altitude. It is initialized on 22 August 1999 at 0000 UTC and is integrated forward for 30 hours. More details on the simulation are given by *Nuissier* [2003] and O. Nuissier et al. (A numerical simulation of Hurricane Bret on 22–23 August 1999 initialized with airborne Doppler radar and dropsonde data, *Quarterly Journal of the Royal Meteorological Society*, 2004) (hereinafter referred to as Nuissier et al., submitted manuscript, 2004). The case SACZ has been simulated with three nested models, with a horizontal grid spacing of 36, 12, and 3 km. The vertical grid has 84 levels with a level spacing of 80 m close to the surface to 300 m at high altitude. The inner grid covers 582 km × 726 km. It is initialized on 6 February 2001 at 1200 UTC and is integrated forward for 27 hours.

### 2.1. General Description of the Mixed-Phase Microphysical Scheme

[11] The calculations essentially follow the approach of *Lin et al.* [1983]: A three-class ice parameterization is used

**Table 1.** General Characteristics for the Meso-NH Simulations

| | Bret Hurricane Case | SACZ Case |
|---|---|---|
| Initialization time | 0000 UTC, 22 Aug. 1999 | 1200 UTC, 6 Feb. 2003 |
| Nesting geometry | 4 models | 3 models |
| Nested grid spacing | 55, 14, 5, 1.67 km | 36, 12, 3 km |
| Vertical grid | 44 stretched levels from 80 m to 600 m | 84 stretched levels from 30 m to 300 m |
| Vertical grid used by ATM | every level | every second level |
| Model top | 20 km | 20 km |
| | Physical Parameterizations[a] | |
| Microphysics | bulk scheme, 6 water categories: water vapor, cloud water, rain water, cloud ice, snow, graupel [*Pinty and Jabouille*, 1998] | |
| Radiation | ECMWF package [*Morcrette*, 1991] | |
| Turbulence | 1.5-order scheme [*Cuxart et al.*, 2000] | |
| Surface | ECMWF sea surface temperature and Charnock roughness length | |

[a]Physical parameterizations given are for the high-resolution model. Physical parameterizations for the coarse resolution models are the same, but with the addition of a convective scheme [*Bechtold et al.*, 2001].

with a *Kessler*'s [1969] scheme for the warm processes. As illustrated in Figure 1, the scheme predicts the evolution of the mixing ratios of six water species: $r_v$ (vapor), $r_c$, and $r_r$ (cloud droplets and rain drops) and $r_i$, $r_s$, and $r_g$ (pristine ice, snow/aggregates, and frozen drops/graupel defined by an increasing degree of riming). The concentration of the pristine ice crystals, here assumed to be plates, is diagnosed. The concentration of the precipitating water drops, snow, and graupels is parameterized according to *Caniaux et al.* [1994], with the total number concentration $N$ given by

$$N = C\lambda^x, \tag{1}$$

where $\lambda$ is the slope parameter of the size distribution, and $C$ and $x$ are empirical constants derived from radar observations. The size distribution of the hydrometeors is assumed to follow a generalized $\gamma$-law:

$$n(D)dD = Ng(D)dD = N\frac{\alpha}{\Gamma(\nu)}\lambda^{\alpha\nu}D^{\alpha\nu-1}\exp(-(\lambda D)^{\alpha})dD, \tag{2}$$

where $g(D)$ is the normalized form which reduces to the Marshall-Palmer law when $\alpha = \nu = 1$ ($D$ is the diameter of the drops or the maximal dimension of the particles). Finally, simple power laws are taken for the mass-size ($m = aD^b$) and for the velocity-size ($v = cD^d$) relationships to perform useful analytical integrations using the moment formula:

$$M(p) = \int_0^\infty D^p g(D)dD = \frac{\Gamma(\nu + p/\alpha)}{\Gamma(\nu)}\frac{1}{\lambda^p}, \tag{3}$$

where $M(p)$ is the $p$th moment of $g(D)$. A first application of equation (3) is to compute the mixing ratio $r_x$ as

$$\rho r_x = aNM_x(b). \tag{4}$$

Table 2 provides the complete characterization of each ice category and cloud droplets/raindrops.

**Table 2.** Characteristics of Each Hydrometeor Category[a]

| Parameters | $r_i$ | $r_s$ | $r_g$ | $r_c$ | $r_r$ |
|---|---|---|---|---|---|
| $\alpha$ | 3 | 1 | 1 | 3 | 1 |
| $\nu$ | 3 | 1 | 1 | 3 | 1 |
| $a$ | 0.82 | 0.02 | 196 | 524 | 524 |
| $b$ | 2.5 | 1.9 | 2.8 | 3 | 3 |
| $c$ | 800 | 5.1 | 124 | | 842 |
| $d$ | 1.00 | 0.27 | 0.66 | | 0.8 |
| $C$ | | 5 | $5 \times 10^5$ | | $10^7$ |
| $x$ | | 1 | $-0.5$ | | $-1$ |

[a]Coefficients $\alpha$ and $\nu$ are used in equation (2). The other coefficients are related to power law relationships for the mass ($m = aD^b$) and the fall speed ($v = cD^d$), where $D$ is the particle size, and for the concentration in equation (1). All variables are in MKS units.

### 2.2. Sources and Sinks of Hydrometeors

[12] Hydrometers are formed and destroyed according to the processes depicted in Figure 1. The warm part of the scheme (Kessler scheme) includes the growth of cloud droplets by condensation (CND) and the formation of rain by autoconversion (AUT). Raindrops grow by accretion (ACC) or evaporate in subsaturated areas (EVA).

[13] In the cold part of the scheme, the pristine ice category is initiated by homogeneous nucleation (HON)

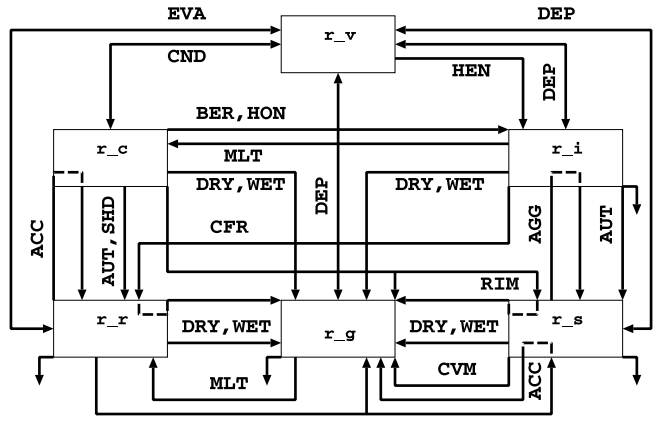


**Figure 1.** Microphysical processes included in the mixed-phase scheme (see section 2.2 for the acronyms and explanations).

when $T \leq -35°C$, or more frequently by heterogeneous nucleation (HEN), so the small ice crystal concentration is a simple function of the local supersaturation over ice. These crystals grow by water vapor deposition (DEP) and by the Bergeron-Findeisen effect (BER). The snow phase is formed by autoconversion (AUT) of the primary ice crystals; it grows by deposition (DEP) of water vapor, by aggregation (AGG) through small crystal collection and by the light riming produced by impaction of cloud droplets (RIM) and of raindrops (ACC). Graupel are formed as a consequence of the heavy riming of snow (RIM and ACC) or by rain freezing (CFR) when supercooled raindrops come in contact with pristine ice crystals. Distinction between light and heavy riming is made on the basis of a critical size of the snowflake (droplets) or by estimation of the mean density of the resulting particle (raindrops). According to the heat balance equation, graupel can grow more efficiently in the (WET) mode than in the (DRY) mode when riming is very intense (as for hailstone embryos). In the latter case, the excess of nonfreezable liquid water at the surface of the graupel is shed (SHD) to form raindrops. When $T \geq 0°C$, pristine crystals immediately melt into cloud droplets (MLT) while snowflakes are progressively converted (CVM) into graupel which melt (MLT) as they fall. Each condensed water species has a nonzero fall speed except for cloud droplets.

## 3. ATM Radiative Transfer Model

[14] The microwave radiative transfer model used in this work combines both gas absorption and hydrometeors scattering. The basic transfer equation is

$$\mu \frac{dI(z,\mu,\varphi)}{dz} = K(z,\mu,\varphi)I(z,\mu,\varphi) - \int_{-1}^{1} d\mu' \int_{0}^{2\pi} d\varphi' Z \cdot (z,\mu,\varphi,\mu',\varphi')I(z,\mu',\varphi') - \sigma(z,\mu,\varphi)B[T(z)], \quad (5)$$

where $I = (I, Q, U, V)^T$ is the Stokes vector fully describing the radiation field at a given position (z, in the plane-parallel geometry we will consider, see below) and for a given orientation (defined by $\mu = \cos(\vartheta)$ and $\varphi$ in spherical coordinates), $K$ is the extinction matrix, $Z$ is the $4 \times 4$ phase matrix, $\sigma$ is the $4 \times 1$ emission vector, and $B(T)$ is the blackbody radiance at temperature $T$. The frequency dependence of $I$, $K$, $Z$, $\sigma$, and $B$ is implicit. The extinction matrix describes the pure signal extinction in a given direction for the different polarization components of the radiation. The phase matrix relates the Stokes parameters of a scattered beam in the direction $\vartheta$, $\varphi$ with respect to the input direction $\vartheta'$, $\varphi'$. It applies in principle to a single scattering particle. However, for a small volume with randomly located and oriented particles separated by distances such that each particle is in the far field of the others, the waves scattered by different particles are random in phase and their Stokes parameters add up. As a consequence, the phase matrix of a volume element is the sum of the individual particle phase matrices [*Mishchenko et al.*, 1995]. The term containing the emission vector in equation (5) describes the emission of radiation in the media. It is proportional to $B(T)$: Thermal emission is the only source of radiation. The extinction and phase matrices and the emission vector are related according to

$$K_{i1}(z,\mu,\varphi) = \int_{-1}^{1} d\mu' \int_{0}^{2\pi} d\varphi' Z_{i1}(z,\mu,\varphi,\mu',\varphi') + \sigma_i(z,\mu,\varphi), \quad i = 1,\ldots,4, \quad (6)$$

as a consequence of the detailed energy balance.

[15] The absorption by atmospheric gases is introduced in the model according to *Pardo et al.* [2001]. The far-field phase matrices of an ensemble of spherical or nonspherical particles are computed using T-matrix codes (TMD) developed by *Mishchenko* [1991, 1993, 2000]. In this work, spherical particles are considered but the case of partially oriented nonspherical particles (provided that the orientation is random at least in azimuth) can be treated [*Mishchenko*, 2000; *Prigent et al.*, 2001]. The original TMD routines were written for well known particle size distributions (e.g., log-normal or modified gamma). For this study, the model has been modified to take into account the presence of multiple particle types in a given atmospheric layer (see next section).

[16] The radiative transfer problem is considered azimuthally symmetric (plane parallel geometry). In this case, the Stokes parameters $U$ and $V$ vanish [*Evans and Stephens*, 1995], and equation (5) reduces to

$$\mu \frac{dI^0(z,\mu)}{dz} = K(z,\mu)I^0(z,\mu) - 2\pi \int_{-1}^{1} d\mu' Z^0(z,\mu,\mu')I^0(z,\mu') - \sigma(z,\mu)B[T(z)], \quad (7)$$

where the superscript 0 denotes the zeroth azimuthal harmonic of the concerned quantity, all matrices represent the upper left $2 \times 2$ blocks of the respective $4 \times 4$ matrices appearing in equation (5), and all column vectors have the dimension 2 and are composed of the upper two elements of the respective 4-element column vectors in the same equation. This $2 \times 2$ equation is then integrated using the doubling and adding method [*Evans and Stephens*, 1995].

[17] The numerical calculations face several quadratures that impact their accuracy and CPU time. First, the atmosphere is divided into a number of layers ($NQ_A$). For each channel the result is the average over the frequency band ($NQ_B$ frequencies depending on the spectral dependence in the studied region). For each frequency, there is an angular quadrature to compute the phase matrix of a single particle ($NQ_C$ angles). In each atmospheric layer, several types of particles coexist ($NQ_D$), with a size distribution ($NQ_E$ particle sizes are considered). This calculation is valid for any output direction only if the particle is spherical. For the nonspherical particle case, two new quadratures, in azimuth and elevation ($NQ_F$, $NQ_G$), must be introduced. Finally, in the integration of the radiative transfer equation using the doubling and adding method, another angular quadrature is necessary: The number of input and output angles considered at the boundaries between different atmospheric layers, $NQ_H$. The typical values used in this work for each quadrature are as follows: $NQ_A = 44$ and 40 for Hurricane Bret and for the SACZ respectively, $NQ_B = 1$, $NQ_C = 19$,

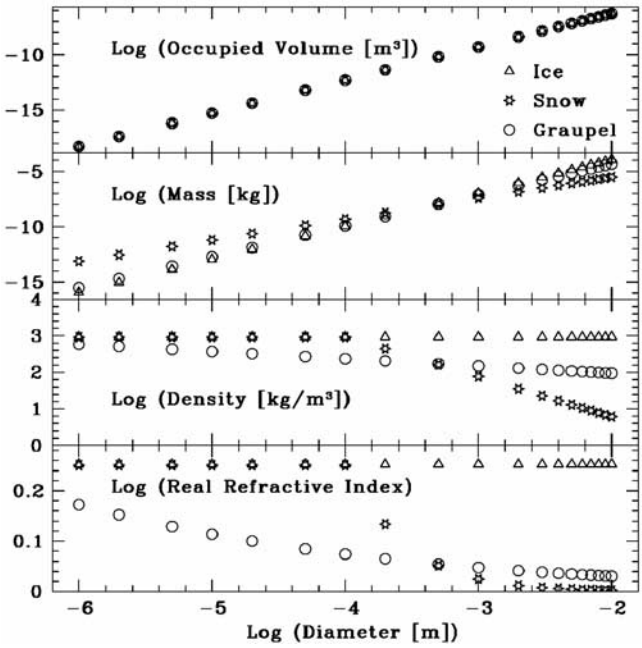


**Figure 2.** Physical properties of frozen hydrometeors as a function of their diameter.

$NQ_D = 5$, $NQ_E = 4$, $NQ_F = NQ_G = 1$ (we only consider spherical particles), and $NQ_H = 8$.

## 4. Interfacing the ATM Radiative Transfer Code and the Meso-NH Cloud Output

[18] For this specific study, the most important change performed on the initial ATM code as used by *Prigent et al.* [2001] is to allow accurate scattering calculations when several hydrometeor species are simultaneously present in a given layer. The different physical properties and distributions of the 5 types of hydrometeors defined by Meso-NH have to be taken into account, in order to perform the microwave radiative transfer for conditions that are as consistent as possible with the Meso-NH simulations. The interfacing work is presented in this section. The impacts of several parameters on the calculated brightness temperatures are also discussed.

### 4.1. Particle Dielectric Properties

#### 4.1.1. Description of the Particle Dielectric Properties

[19] Five types of hydrometeors are considered in Meso-NH: cloud (droplets), rain, (cloud) ice, snow, and graupel. Cloud droplets and ice cloud particles are expected to be small compared to the wavelength of our observations and are hence attributed a fixed diameter and density of 20 μm and 1 g cm$^{-3}$ for cloud droplets and 60 μm and 0.92 g cm$^{-3}$ for cloud ice. These values were also selected by the International Satellite Cloud Climatology Project [*Rossow and Schiffer*, 1999]. The precipitating hydrometeors have a distribution of sizes of diameter D and masses m given by

$$m = aD^b, \tag{8}$$

where $a$ and $b$ depend on the type of hydrometeor and are listed in Table 2. The densities ρ are determined by

$$\rho = \frac{m}{(\pi/6)D^3} = \frac{6}{\pi} aD^{b-3}. \tag{9}$$

However, we have limited the density to values less than 1 g cm$^{-3}$ for rain and 0.92 g cm$^{-3}$ for ice and graupel, which means that there is a cutoff at radii where the density becomes that of water/ice.

[20] The refractive index for liquid water seems to be well understood and is taken from *Manabe et al.* [1987] for rain and cloud droplets. For ice the refractive index ($n = (EM1 + iEM2)^2$) is taken from *Warren* [1984]:

$$EM1_{ice} = 3.093 + 0.72 \times 10^{-4} * T + 0.11 \times 10^{-5} * T^2, \tag{10}$$

$$EM2_{ice} = 2.0 * 0.002 * \sqrt{EM1_{ice}}, \tag{11}$$

with $T$ the temperature of the particles. The refractive indexes of dry snow and porous ice are described by *Ulaby et al.* [1986] and agree well with the measurements of ground based ice. Hence their formulas for snow and graupel are used:

$$EM1 = (1. + 0.51 * \rho)^3, \tag{12}$$

$$EM2 = \frac{0.34 * (\rho/0.916) * EM2_{ice}}{\left(1 - 0.417 * (\rho/0.916)^2\right)}, \tag{13}$$

where ρ is density in g cm$^{-3}$. The refractive index changes slowly for graupel, but very abruptly for snow at diameters between 1 mm and 100 μm (see Figure 2, where the calculations are performed for $T$ = 270 K). Realistic sizes for most precipitating particles are between 100 and 1000 μm. Melting particles are considered as wet graupels. Shed water from these particles lead to the formation of rain drops.

[21] Figure 2 summarizes the dependence of volume, mass, density, and the real part of the refractive index as a function of diameter on a log-log scale for the frozen hydrometeors.

#### 4.1.2. Effect of the Particle Dielectric Properties on the Brightness Temperature

[22] The brightness temperature is extremely sensitive to the real part of the refractive index, even if it varies only very little. Changes of 10% in the refractive index can result in brightness temperature differences over 100%. To investigate the effect of changes in density (and hence in the refractive index) in a realistic case, a typical vertical profile was selected from the moist ring of Hurricane Bret (1.7 kg m$^{-2}$ of cloud droplets, 13 kg m$^{-2}$ of rain, 0.7 kg m$^{-2}$ of cloud ice, 9 kg m$^{-2}$ of graupel and 3.9 kg m$^{-2}$ of cloud droplets) and the brightness temperature is calculated, first using a density which varies with diameter as described above and second with fixed densities of 0.1 g cm$^{-3}$ for snow and 0.4 g cm$^{-3}$

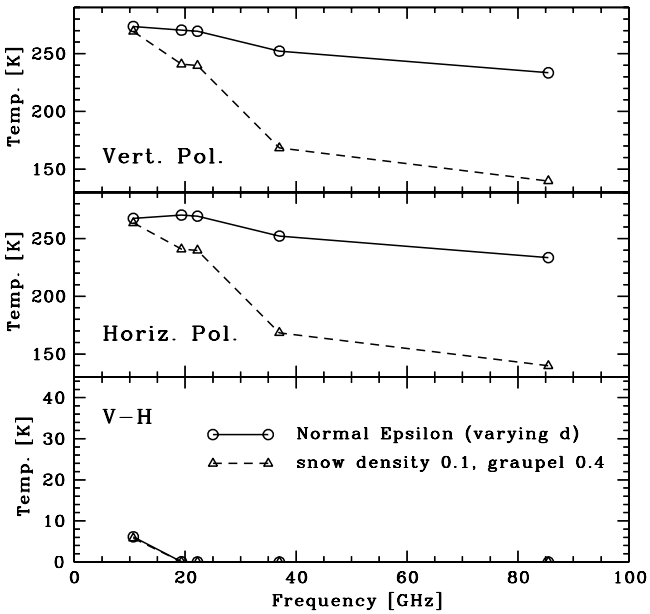


**Figure 3.** Effect of a constant density versus a varying one on the brightness temperature (see section 4.1.2).

for graupel, which are standard values found in the literature [*Pruppacher and Klett*, 1997] (Figure 3). Using a fixed density independent of particle size reduces the brightness temperature by as much as 100 K at 85 GHz. This is due to the fact that the fixed density is higher than the variable density for particles larger than 1 mm. Since there are quite a few of these large particles in the intensely precipitating ring of the hurricane, the fixed density raises the real refractive index and hence the scattering, thereby reducing the brightness temperature especially at the higher frequencies (37 and 85 GHz). For a realistic prediction of the brightness temperatures it is therefore crucial to classify the hydrometeors into different types and to take their different physical properties into account. In particular, the best available model for the density and the refractive index of each type of hydrometeors should be used.

### 4.2. Particle Distribution

#### 4.2.1. Description of Particle Size Distribution

[23] The size distributions of precipitating particles defined in Meso-NH, described in section 2.1 and characterized by their respective slope parameter $\lambda$ (Table 2), are used as inputs for ATM. Figure 4 gives an example of the particle distribution of 10 g $m^{-3}$ of snow, graupel, and ice. Since cloud ice is modeled to have a single diameter of 60 $\mu$m, it shows as a single point in each diagram. In contrast, snow and graupel follow an exponentially decreasing distribution (top plot), which, multiplied by their masses (middle plot), results in a bell-shaped curve (bottom plot). The particles, which make up most of the mass (maximum in bottom plot), have a diameter $D_{mod}$ of $b/\lambda$, with $b$ and $\lambda$ as defined in section 2.1 in the case of Marshall-Palmer distribution laws. This diameter $D_{mod}$ depends on the amount of hydrometers (in kg $m^{-3}$), as well as on the hydrometeor type, as can be seen in Figure 4.

[24] In order to minimize the computation cost, which is particularly high for calculating the scattering matrix, we characterize the particle distribution for each kind of precipitating hydrometeor by 4 diameters and their corresponding number distribution. The 4 characteristic diameters are chosen to be 1/4, 3/4, 1.5 and 3 $\times$ $D_{mod}$ and the number of particles is derived from the integrated mass of each bin divided by the mass of a particle with the median diameter of the bin integrated over. More precisely we sum over 100 points in each bin rather than integrate, but the error due to this approximation is less than 2% in total mass.

#### 4.2.2. Effect of Particle Size Distribution on the Brightness Temperature

[25] As we expect $T_B$ to be sensitive to the total number of particles, it is worth examining the effects of changing the parameters $C$ and $x$ of the size distribution (equation (1)). We found that this modification has only a small effect on the brightness temperatures. For example, describing rain with the $C$ and $x$ values of graupel, will only change the resulting brightness temperature by a few degrees. A larger effect is found in the extreme case of changing all $C$ and $x$ values to that of snow (which has a significantly smaller $C$ and larger $x$, see Table 2). For a typical integrated hydrometeor column in a hurricane (same example as described in section 4.1.2) the modeled brightness temperature was reduced by about 10 K for the lower frequencies between 10 and 40 GHz and by

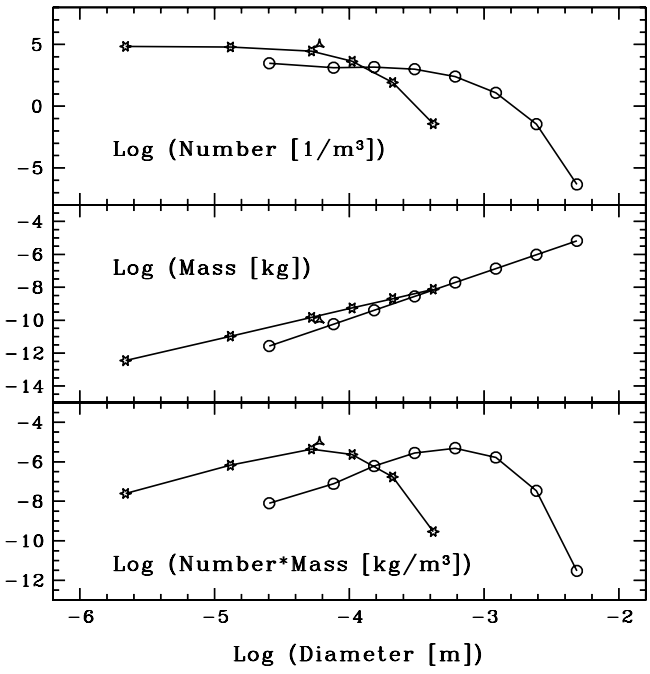


**Figure 4.** Particle distribution for ice (triangles), snow (stars), and graupel (circles). The top plot shows the distribution of the number of particles with diameter, the middle plot shows the mass of an individual particle as a function of its diameter, and the bottom plot shows the number $\times$ mass of the different types of hydrometeors as a function of diameters. All plots are on a log-log scale.

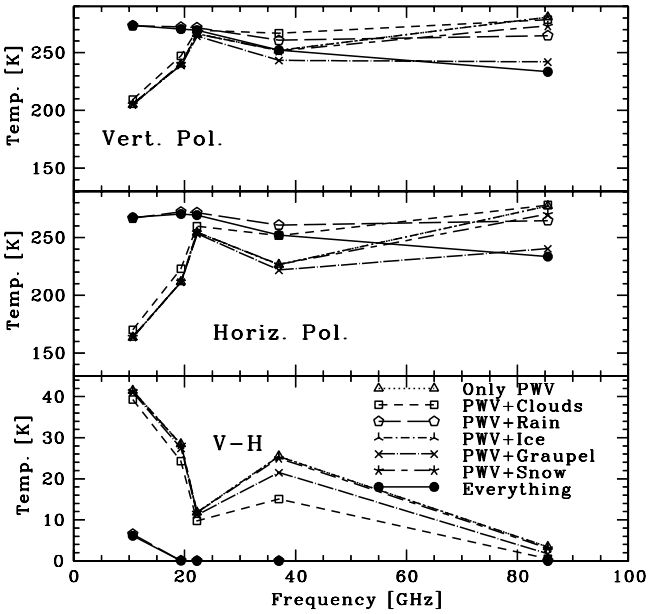


**Figure 5.** Contribution of each hydrometeor to the brightness temperature as well as that of only PWV and all hydrometeors together.

about 50 K at 85 GHz. Though the parameterization of the particle distributions are relatively well understood, uncertainties in the classification of the type of hydrometeors (e.g., is frozen water in the form of snow or graupel?) has a similar effect and may well contribute to an uncertainty in the brightness temperature.

### 4.3. Combined Effect of Particle Properties, Dielectric Properties, and Size Distribution on the Brightness Temperature

[26] Figure 5 demonstrates the effect of each different type of hydrometeors on the brightness temperature for the case discussed in section 2.1. The seven curves show the brightness temperatures that would result from the presence of a single hydrometeor category for vertical and horizontal polarizations as well as their polarization differences (in all cases, emission from precipitable water vapor (PWV) and the surface are included). PWV on its own shows increasing emission with frequency with the exception of 22 GHz, where there is a water vapor emission line. The large difference in polarization is due to the emission of the ocean. Liquid water (rain and cloud droplets) increases the brightness temperature especially at lower frequencies, whereas frozen water (ice, snow, and graupel) introduces scattering, which reduces the brightness temperature especially at the higher frequencies. Since the frozen particles are assumed to be spherical they do not increase the difference in polarization, as would oblate or prolate oriented particles [*Prigent et al.*, 2001]. This is a simplification when considering snowflakes or big precipitating drops. The model using all hydrometeors shows strong emission at all frequencies, but reduced brightness temperatures at higher frequencies due to scattering. The polarization difference is nonzero only at 10 GHz, as -in this very moist example- this is the only frequency where the atmosphere is partly transparent and the ocean emissivity contributes to the overall brightness temperature.

### 4.4. Wind and Surface Emissivity

#### 4.4.1. Description of Wind and Surface Emissivity

[27] In contrast to the surface emissivity of land, the emissivity of the ocean can be modeled with some confidence. The sea emissivity depends essentially on wind speed above the ocean. Models agree well with measurements up to wind speeds of $\sim$25 m s$^{-1}$ [*Guillou et al.*, 1996], but extrapolations to higher wind speeds become inaccurate because of the lack of validation measurements at higher wind speeds. Using the surface temperature and the wind speed of the lowest atmospheric layer provided by Meso-NH we calculate the emissivity of the ocean for each grid point. For wind speeds higher than 25 m s$^{-1}$ the 25 m s$^{-1}$ emissivity value is used. As high winds usually coincide with high column densities of hydrometeors, errors in the surface emissivity are likely to be masked by the strong emission from the hydrometeors and should not introduce large errors in the brightness temperature.

#### 4.4.2. Effect of Wind and Surface Emissivity on the Brightness Temperature

[28] The effect of the surface emissivity can be better observed in cloud-free regions or at the edge of convective structures where the column density of the hydrometeors is low and allows the satellite to probe the surface. Figure 6 shows the effect of different wind speeds on the brightness temperature for horizontal and vertical polarizations as well as their difference for a location at the edge of Hurricane Bret (0.1 kg m$^{-2}$ of cloud droplets, 0 kg m$^{-2}$ of rain, 0.3 kg m$^{-2}$ of ice, 0.08 kg m$^{-2}$ of graupel and 0.7 kg m$^{-2}$ of snow). The emissivity in both linear polarizations rises with increasing wind speed, but more in the horizontal than in the vertical polarization. The increase in brightness temperature is not linear, but quicker at higher wind speeds. It is therefore essential to know the wind speed above the

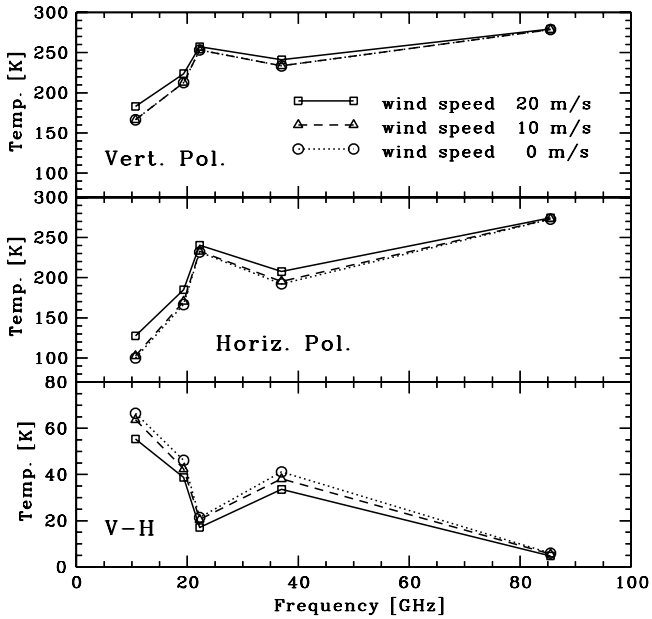


**Figure 6.** Effect of surface wind speeds on the brightness temperature for both polarizations.

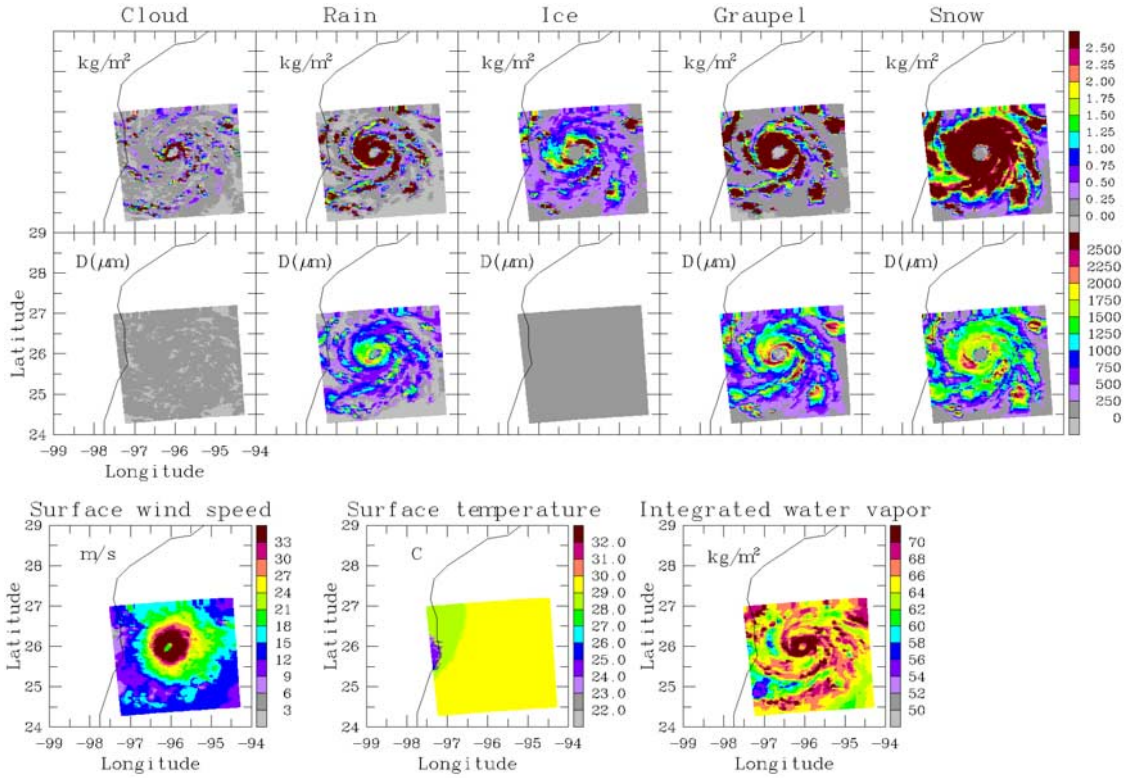


**Figure 7.** Meso-NH fields of Hurricane Bret on 22 August 1999, 1600 UTC. Upper panels: integrated hydrometeor contents for each species. Middle panels: the maximum of the mode value of the hydrometeor distribution diameter. Lower panels: from left to right, the surface wind speed, the surface skin temperature, and the integrated water vapor.

ocean well in order to accurately predict the brightness temperature, especially for areas of low water column densities, low frequencies, and strong wind regimes.

## 5. Comparisons of Simulations With the Observations From TRMM Microwave Instrument (TMI)

### 5.1. TRMM Microwave Instrument

[29] The Tropical Rainfall Measuring Mission (TRMM) is the first mission dedicated to observing and quantifying precipitation in the Tropics. It is a joint National Aeronautics and Space Administration (NASA) and National Space Development Agency of Japan (NASDA) effort. For a detailed description of the TRMM instruments, see http://trmm.gsfc.nasa.gov.

[30] The TMI (TRMM Microwave Instrument) measures the microwave radiation emitted by the Earth and its atmosphere, at five separate frequencies, 10.65, 19.35, 21.30, 37.00, 85.50 GHz, for both vertical and horizontal polarizations, except for the 21.30 GHz channel that is only observed in vertical polarization. From a satellite altitude of 350 km, TMI has a 780 km wide swath on the surface and the spatial resolution ranges from 36.8 km $\times$ 63.2 km at 10.65 GHz to 4.6 km $\times$ 7.2 km at 85.50 GHz.

[31] The TMI data used in this study are the 1B calibrated microwave brightness temperatures extracted from the NASA DAAC (http://lake.nascom.nasa.gov/data/dataset/TRMM).

### 5.2. Comparisons Between the Observed and Simulated Brightness Temperature Fields

#### 5.2.1. Hurricane Bret

[32] The TMI instrument overflew Hurricane Bret at several occasions. The overpassing at 1642 UTC on 22 August 1999 is selected for the comparison with the simulations, as it is closest in time with the Meso-NH simulations at 1600 UTC on the same day.

[33] Figure 7 presents the Meso-NH simulated integrated hydrometeor fields at 1600 UTC, i.e., at T0 + 16h (upper panels). At that time, the hurricane has just reached the coast. For each grid box, each atmospheric layer, and each hydrometeor type, the mode value of the hydrometeor distribution diameter is estimated. For each grid box and each hydrometeor type, the maximum of this mode value in the atmospheric column is shown (middle panels). Constant particle sizes are used for cloud droplets and cloud ice, as already discussed (see section 4.1.1). For graupel and snow, the particle sizes can reach large values (mode values over 2 mm in diameter) and are associated with large ice water path. As a consequence, strong scattering is expected for the higher TMI frequencies. The lower panels on Figure 7 show the surface wind speed, the surface skin temperature, and the integrated water vapor.

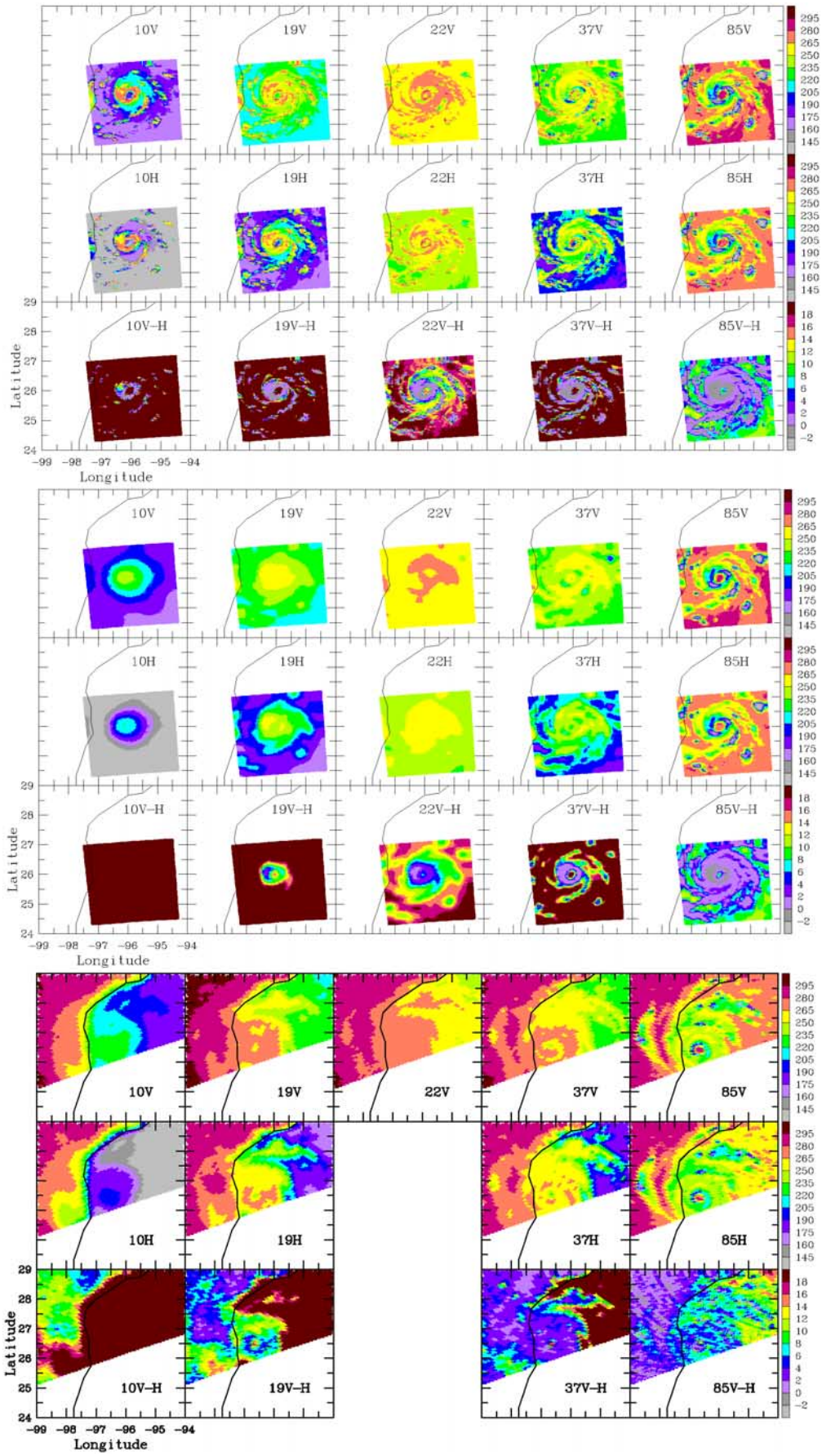
10V
19V
22V
37V
85V
10H
19H
22H
37H
85H
10V–H
19V–H
22V–H
37V–H
85V–H
295 280 265 250 235 220 205 190 175 160 145
18 16 14 12 10 8 6 4 2 0 –2
Latitude
29 28 27 26 25 24
–99 –98 –97 –96 –95 –94
Longitude

**Figure 8.**

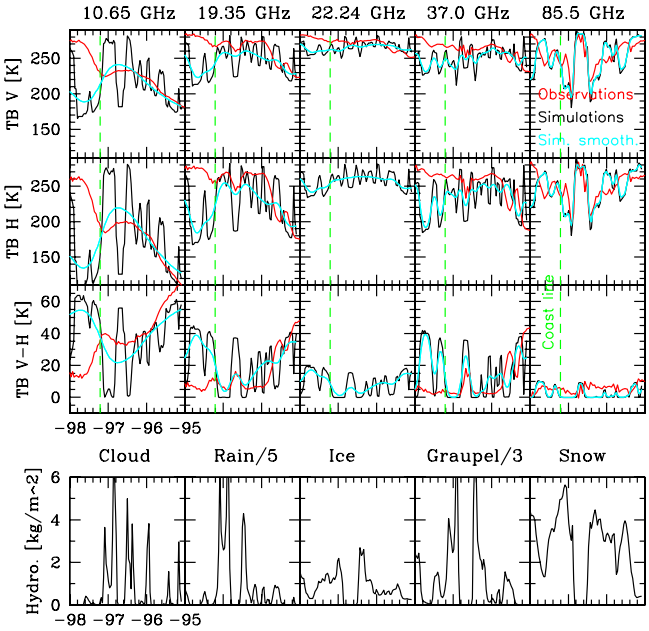


**Figure 9.** Cross section of the simulation of Hurricane Bret at latitude 26°N (at Meso-NH nominal resolution, in black) and convoluted with the antenna pattern (in blue) along with the corresponding cross section in the TMI observations (in red). The integrated hydrometeors as simulated by Meso-NH are also presented.

[34] Microwave $T_B$ are obtained for each grid box using the ATM model interfaced with Meso-NH output as previously described. The simulated $T_B$ are presented on Figure 8, at the nominal Meso-NH grid resolution of 1.67 km (upper panels), for all the TMI frequencies for both linear polarizations. The polarization differences are also displayed. The simulated fields convolved with a Gaussian function that is close to the actual TMI antenna patterns for each frequency are shown on Figure 8 (middle panels). The effect of the antenna pattern increases with decreasing frequencies, as expected, because of the lower resolution of the radiometer at lower frequencies (from 36.8 km × 63.2 km at 10.65 GHz to 4.6 km × 7.2 km at 85.50 GHz). The surface wind speed impacts the microwave signal in the gaps between the hurricane spiral bands, especially at lower frequencies. Water vapor contents are large, resulting in warm $T_B$ everywhere at 22 GHz.

[35] The TMI observations 1642 UTC on 22 August are presented on the lower panels in Figure 8. The 9 TMI channels, along with the polarization difference for frequencies for which the two linear polarizations are measured, are shown. Because of the 42 min time shift the hurricane has moved toward the west with respect to the simulation at 1600 UTC and has already reached the Texan coast, close to the border with Mexico.

[36] The antenna convolved simulated $T_B$ fields (middle panels) show spatial structures that are very similar to the observed ones. In particular, the spiral structure of the hurricane is clearly observed, especially at 85 GHz, where the satellite has the highest spatial resolution. Over the ocean at the eastern edge of the hurricane, the simulated $T_B$ are low, especially at the lower frequencies, where the ocean surface is characterized by low emissivities and large polarization differences. Conversely, precipitation and clouds in the hurricane act as emitters and absorbers showing warmer $T_B$ over the radiometrically cold ocean at the lower frequencies. At 85 GHz, lower $T_B$ are observed, as a result of scattering by large frozen particles. Observed $T_B$ over land are warmer than over ocean at lower frequencies. The land surface emissivities are high, often close to unity, and the polarization differences are small. Because of high radiances over land, even at low frequencies, $T_B$ are lower over clouds and precipitating areas than over clear skies. Transmission at 85 GHz in the hurricane area is very small meaning that changes in surface properties from ocean to land do not significantly affect the observations at this frequency.

[37] For a more quantitative comparison between observations and simulations, Figure 9 presents the observed and simulated $T_B$, along a section that crosses the hurricane eye at a fixed latitude. For easier comparison, the simulation has been shifted to collocate the observed and simulated hurricane centers (due to the time shift). The corresponding hydrometeor amounts are also shown for the 5 hydrometeor types (lower panels). Note that for display purposes, the rain and graupel integrated contents have been scaled.

[38] There is an overall good agreement between the observations and the simulations of smoothed $T_B$. West of the coast lines, large discrepancies with respect to the observations are due to the different emissivities of land and ocean. As expected, the difference increases with decreasing frequencies. Over ocean east of the hurricane eye, there is a broad underestimation of the $T_B$ at 19, 22, and 37 GHz of the order of 10 K. Closer examination of the simulated $T_B$ at the nominal Meso-NH resolution (black lines on Figure 9) shows that the discrepancy is likely related to an underestimation of the $T_B$ in the regions between the spiral bands of the hurricane where the hydrometeor contents are low. The highest simulated $T_B$ are in good agreement with the observations (red line); however, the lowest simulated $T_B$ (corresponding to gaps between hurricane spiral bands) appear too low. This could be due to an underestimation of the hydrometeor contents outside the spiral bands of the hurricane or to underestimation of the wind simulated by Meso-NH. The surface winds have been compared to dropsonde measurements and they appear realistic (Nuissier et al., submitted manuscript, 2004). In addition, increasing the surface wind speed would lead to an increase in the 10 GHz simulated $T_B$ (and a corresponding decrease in the polarization difference), which is already too

**Figure 8.** Simulated and observed brightness temperature fields for Hurricane Bret. Upper panels: simulated $T_B$ at the nominal Meso-NH grid resolution of 1.67 km, on 22 August 1999 at 1600 UTC, for all the TMI frequencies for both linear polarizations along with the polarization differences. Middle panels: simulated fields convolved with a Gaussian function close to the actual TMI antenna patterns for each frequency. Lower panels: TMI observations on 22 August 1999 at 1642 UTC for the 9 TMI channels, along with the measured polarization differences.

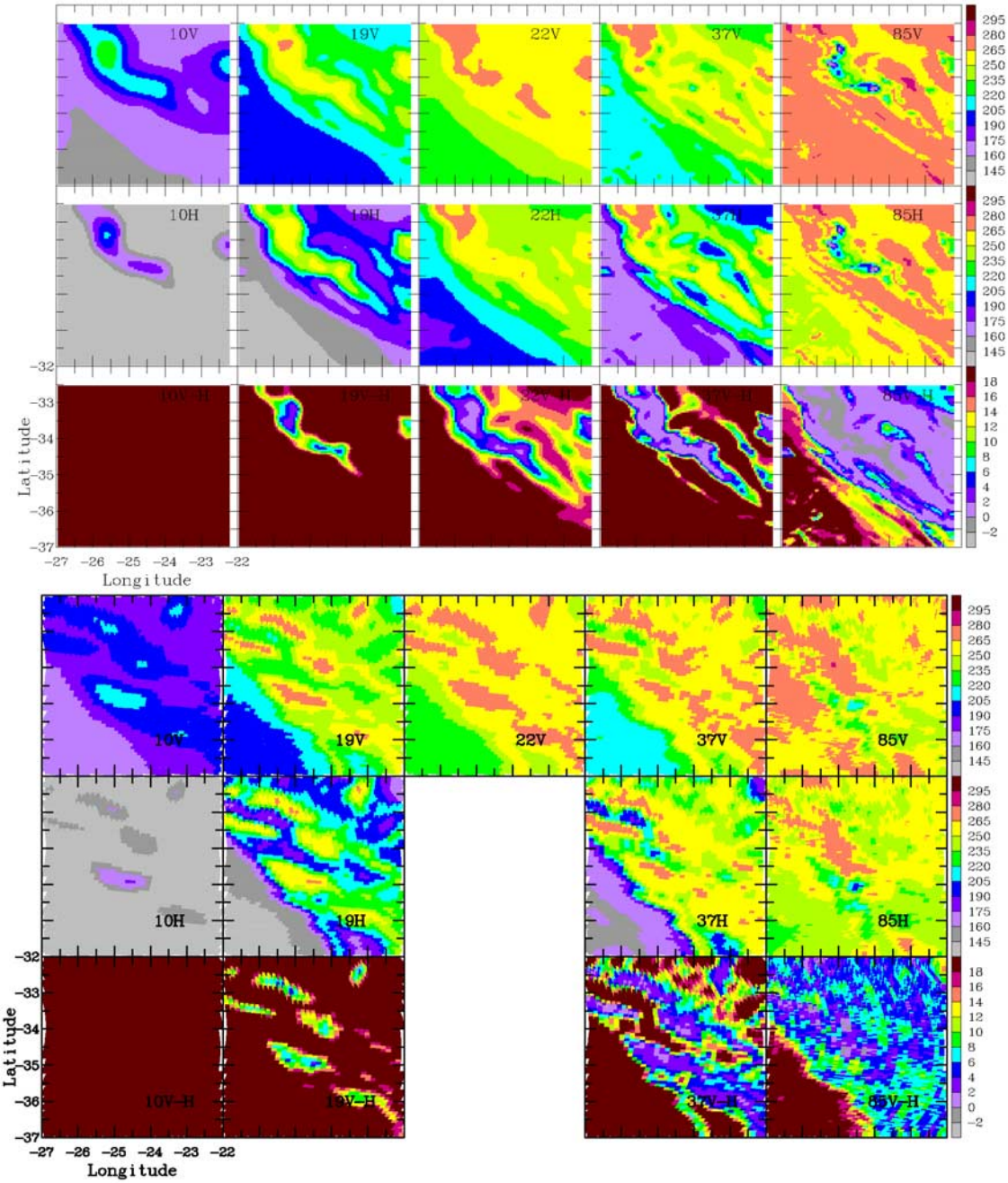


**Figure 10.** Simulated and observed brightness temperature fields for the South Atlantic Convergence Zone case on 7 February 2001 at 1500 UTC. Upper panels: simulated $T_B$ fields convolved with a Gaussian function close to the actual TMI antenna patterns for each channel and for the polarization differences. Lower panels: TMI observations on 7 February 2001 at 1214 UTC for the 9 TMI channels, along with the measured polarization differences.

high (respectively too low) as compared to the observations. The 85 GHz channel simulations (which are extremely sensitive to the characteristics of the particle ice phase, see section 4) are in very good agreement with the observations.

[39] Two features in Figure 9 deserve further comments. First, in the area of maximum graupel content in the cross section (longitude 96.4°E and 96.9°E), the 85 GHz $T_B$ are underestimated. A slight underestimation can be noted at the same location in the 37 GHz channel as well. This can be related to an overestimation of the graupel content in these regions, and/or to a mischaracterization of the graupel properties (sizes, density, or related dielectric properties). The kind of agreement found here exemplifies the difficulty for obtaining locally accurate ice-content values with explicit cloud models. It is still a challenge to predict detailed cloud fields with bulk microphysical schemes. Second, the polarization differences at 85 GHz are almost zero in the simulations outside the hurricane eye, whereas non zero differences (~5–10 K) are observed. Polarized radiation at

85 GHz has already been observed in convective areas with the Special Sensor Microwave/Imager and this signature has been interpreted in terms of non spherical oriented particles [*Prigent et al.*, 2001]. For simplicity, only spherical particles have been considered here. No information on the particle shapes and orientations can be used. As a consequence, negligible polarization differences are obtained.

#### 5.2.2. South Atlantic Convergence Zone (SACZ) Case

[40] The second case corresponds to a convective line located in the South Atlantic Convergence Zone (SACZ) off the Brazilian coast, on 7 February 2001. Meso-NH output at 1500 UTC, after 27 hours of simulation, are used as inputs for the radiative transfer model, at 3 km spatial resolution. Again, the simulated $T_B$ are convolved with the TMI antenna patterns at each frequency and the results are displayed in Figure 10 (upper panels). TMI observations at 1214 UTC are presented (lower panels) for all channels along with the polarization differences when available. Strong southwest/northeast gradients are observed in the brightness temperatures, especially for the four lower frequencies, indicating a strong gradient in both wind speed, water vapor path, and hydrometeor content. Simulated and observed brightness temperatures exhibit very similar geographical patterns, with similar $T_B$ values. A shift of $\sim 1^\circ$ northward can be seen between the observations and the simulations, consistent with the time difference between the observations and the simulation. An underestimation of the $T_B$ at 85 GHz can be noticed along the convective line. It is possibly related to an overestimation of the scattering by large particles or by an excess of the convective line intensity as modeled by Meso-NH.

[41] Figure 11 shows a cross section of the observed and the simulated $T_B$. To account for the time difference between the two, the cross section is cut at a constant latitude of 35°S for the observations and at 34°S for the simulations. In general, the agreement is very good for all channels, meaning that the overall structure of the atmospheric fields is well captured by the Meso-NH simulation. As in the previous case, the brightness temperature polarization difference is underestimated by the simulation at 10.65 GHz. This can be related to limitation brought by the sea surface emissivity model. The latter is based on a geometric approach that only considers large-scale surface roughness, and has been validated for frequencies above 18 GHz [*Guillou et al.*, 1996]. As expected, this approach might be no longer valid at lower frequencies where the geometric approximation is questionable. A more comprehensive model could be implemented, superimposing the modeling of a small-scale roughness (capillary waves, small-scale gravity waves) on large-scale undulations (gravity waves) [e.g., *Guissard and Sobieski*, 1987; *Fung et al.*, 1992]. As previously mentioned, a polarization difference at 85 GHz is observed but not simulated. Again, it is likely related to the presence of oriented non spherical particles as already discussed by *Prigent et al.* [2001].

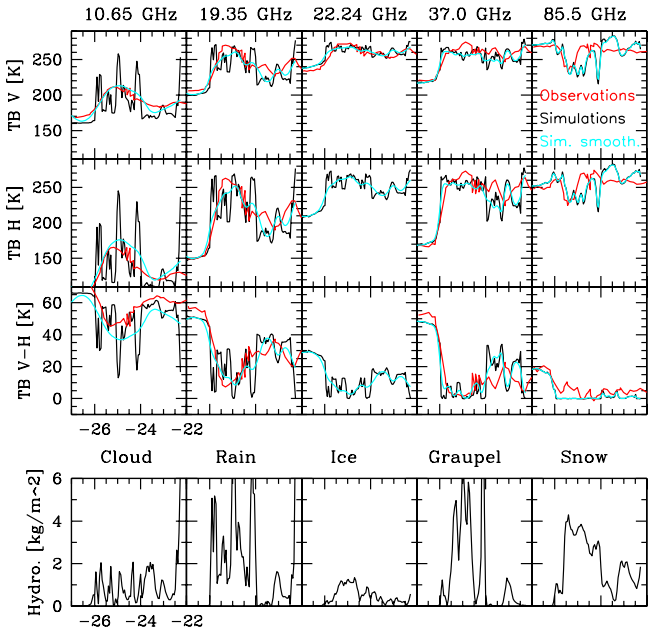


**Figure 11.** Cross section of the simulation of the South Atlantic Convergence Zone case on 7 February 2001 at 1500 UTC at latitude 34°S (at Meso-NH nominal resolution, in black) and convoluted with the antenna pattern (in blue) along with the corresponding cross section in the TMI observations (in red). Integrated hydrometeor columns as simulated by Meso-NH are also presented.

## 6. Conclusion

[42] A microwave radiative transfer model has been developed for accurate simulations of brightness temperature fields using output from the Meso-NH mesoscale model simulations. The radiative transfer code is designed to benefit from a detailed description of the hydrometeor properties as simulated by the Meso-NH model. The sensitivity of the $T_B$ to the hydrometeor properties is carefully analyzed. Synthetic $T_B$ are generated for two contrasted meteorological situations: Hurricane Bret on 22 August 1999 in the Gulf of Mexico and a South Atlantic Convergence Zone case off the Brazilian coast on 7 February 2001. The radiative transfer simulations are compared to the timely corresponding TMI observations on board TRMM, for all frequencies and polarizations. Fitting simulations and observations for the 9 TMI channels is a challenge. Each frequency and polarization is sensitive to a large set of atmospheric and surface parameters. This imposes strong constraints on the quality of both the Meso-NH simulations and the radiative transfer model. Overall, a good agreement is obtained between the simulated and the observed $T_B$ fields, especially for the SACZ case. Differences for the hurricane case are likely to be related to the uncertain quality of the low-level wind forecast. At high frequencies (85 GHz), good agreement is also obtained between the simulations and the observations, given the high sensitivity of these frequencies to appropriate particle characteristics, especially in the ice phase. This is an encouraging result regarding both the accuracy of the radiative transfer model and the overall behavior of the bulk microphysical scheme, especially for the precipitating ice. The present approach carefully combines accurate radiative characteristics for each hydrometeor category, with hydrometeor densities predicted by the state-of-the-art bulk microphysical scheme. The agreement shows that such an approach is consistent.

[43] Simulating passive microwave from mesoscale cloud model output and comparing the results with satellite observations is a powerful tool to diagnose the quality of the cloud fields. The sensitivity of passive microwave to the liquid and ice contents in the clouds makes it possible to quantitatively asses the liquid and ice content generated by the cloud model. The quality of the present comparisons also suggests that assimilating microwave $T_B$ might be feasible in the future for cloud cover and hydrometeor forecasts.

[44] Many more situations have to be analyzed to provide a full assessment of the mesoscale cloud scheme and radiative transfer combination. It is planned to use the microwave simulation tool "online" on a regular basis to systematically evaluate the Meso-NH output. In this study, examples are presented with comparison to TMI observations. Extension to other microwave frequencies is straightforward since the ATM radiative transfer code validity extends up to higher frequencies. For example, comparison with AMSU A and B observations on board NOAA polar satellites could also be performed. As these frequencies are located in absorption lines and are selected to be sensitive to temperature and water vapor profiles of the atmosphere, it would provide a complementary evaluation of the mesoscale cloud model output.

[45] **Acknowledgments.** We would like to thank Bill Rossow for his support in this study. We are very grateful to Mike Mishchenko for providing the T-matrix routines and to Frank Evans for the doubling-adding code. We thank two anonymous reviewers and Michel Desbois for their comments, suggestions, and encouragement. We wish to express our gratitude to F. Roux for his support and to J. Duron for her help in the mesoscale simulations. J. R. Pardo's research is currently supported by Spanish DGES and PNIE grants ESP2002-01627, AYA2002-10113-E and AYA2003-02785-E. Computer resources for Meso-NH simulations have been made available by IDRIS/CNRS (projects 1076 and 569).

## References

Bechtold, P., E. Bazile, F. Guichard, P. Mascart, and E. Richard (2001), A mass flux convection scheme for regional and global models, *Q. J. R. Meteorol. Soc.*, *127*, 869–886.

Caniaux, G., J.-L. Redelsperger, and J.-P. Lafore (1994), A numerical study of the stratiform region of a fast-moving squall line. Part I. General description, and water and heat budgets, *J. Atmos. Sci.*, *51*, 2046–2074.

Chaboureau, J.-P., J.-P. Cammas, P. J. Mascart, J.-P. Pinty, C. Claud, R. Roca, and J.-J. Morcrette (2000), Evaluation of a cloud system life-cycle simulated by Meso-NH during FASTEX using Meteosat radiances and TOVS-3I cloud retrievals, *Q. J. R. Meteorol. Soc.*, *126*, 1735–1750.

Chaboureau, J.-P., J.-P. Cammas, P. J. Mascart, J.-P. Pinty, and J.-P. Lafore (2002), Mesoscale model cloud scheme assessment using satellite observations, *J. Geophys. Res.*, *107*(D16), 4301, doi:10.1029/2001JD000714.

Cuxart, J., P. Bougeault, and J.-L. Redelsperger (2000), A turbulence scheme allowing for mesoscale and large-eddy simulations, *Q. J. R. Meteorol. Soc.*, *126*, 1–30.

Evans, K. F., and G. L. Stephens (1995), Microwave radiative transfer through clouds composed of realistically shaped ice crystals, part II, Remote sensing of ice clouds, *J. Atmos. Sci.*, *52*, 2058–2072.

Fung, A. K., Z. Li, and K. S. Chen (1992), Backscattering from a randomly rough dielectric surface, *IEEE Trans. Geosci. Remote Sens.*, *30*, 356–369.

Guillou, C., S. J. English, and C. Prigent (1996), Passive microwave airborne measurements of the sea surface response at 89 and 157 GHz, *J. Geophys. Res.*, *101*, 3775–3788.

Guissard, A., and P. Sobieski (1987), An approximate model for the microwave brightness temperature of the sea, *Int. J. Remote Sens.*, *8*, 1607–1627.

Kessler, E. (1969), On the distribution and continuity of water substance in atmospheric circulation, *Meteorol. Monogr.*, *10*, *32*, 84 pp.

Kummerow, C., and L. Giglio (1994), A passive microwave technique for estimating rainfall vertical structure information from space. Part I: Algorithm description, *J. Appl. Meteorol.*, *33*, 3–17.

Lafore, J.-P., et al. (1998), The Meso-NH Atmospheric Simulation System. Part I: Adiabatic formulation and control simulations, *Ann. Geophys.*, *16*, 90–109.

Lin, Y.-L., R. D. Farley, and H. D. Orville (1983), Bulk parameterization of snow field in a cloud model, *J. Clim. Appl. Meteorol.*, *22*, 1065–1092.

Manabe, T., H. J. Liebe, and G. A. Hufford (1987), Complex permittivity of water between 0 and 30 THz, paper presented at 12th International Conference on Infrared and Millimeter Waves, Inst. of Electr. and Electron. Eng., Orlando, Fla.

Mishchenko, M. I. (1991), Light scattering by randomly oriented axially symmetric particles, *J. Opt. Soc. Am. A Opt. Image Sci.*, *8*, 871–882.

Mishchenko, M. I. (1993), Light scattering by size/shape distributions of randomly oriented axially symmetric particles of a size comparable to a wavelength, *Appl. Opt.*, *32*, 4652–4666.

Mishchenko, M. I. (2000), Calculation of the amplitude matrix for a nonspherical particle in a fixed orientation, *Appl. Opt.*, *39*, 1026–1031.

Mishchenko, M. I., D. W. Mackowski, and L. D. Travis (1995), Scattering of light by bispheres with touching and separated components, *Appl. Opt.*, *34*, 4589–4599.

Morcrette, J.-J. (1991), Radiation and cloud radiative properties in the European Centre for Medium-Range Weather Forecasts forecasting system, *J. Geophys. Res.*, *96*, 9121–9132.

Mugnai, A., E. A. Smith, and G. J. Tripoli (1993), Foundation for statistical-physical precipitation retrieval from passive microwave satellite measurements. Part II: Emission-source and generalized weighting function properties of a time-dependent cloud-radiation model, *J. Appl. Meteorol.*, *32*, 17–39.

Nuissier, O. (2003), Simulations numériques de cyclones tropicaux à l'aide du modèle Méso-NH, Ph.D. thesis, Univ. Paul Sabatier Toulouse III, Toulouse, France.

Pardo, J. R., J. Cernicharo, and E. Serabyn (2001), Atmospheric Transmission at Microwaves (ATM): An improved model for mm/submm applications, *IEEE Trans. Antennas Propag.*, *49*(12), 1683–1694.

Pinty, J.-P., and P. Jabouille (1998), A mixed-phase cloud parameterization for use in a mesoscale non-hydrostatic model: Simulations of a squall line and of orographic precipitations, paper presented at AMS Conference on Cloud Physics, Am. Meteorol. Soc., Everett, Wash.

Prigent, C., J. R. Pardo, M. I. Mishchenko, and W. B. Rossow (2001), Microwave polarized scattering signatures in clouds: SSM/I observations interpreted with radiative transfer simulations, *J. Geophys. Res.*, *106*, 28,243–28,258.

Pruppacher, H. R., and J. D. Klett (1997), *Microphysics of Clouds and Precipitation*, 2nd ed., Kluwer Acad., Norwell, Mass.

Rossow, W. B., and R. A. Schiffer (1999), Advances in understanding clouds from ISCCP, *Bull. Am. Meteorol. Soc.*, *80*, 2261–2287.

Smith, E. A., A. Mugnai, H. J. Copper, G. J. Tripoli, and X. Xiang (1992), Foundation for statistical-physical precipitation retrieval from passive microwave satellite measurements, part I, Brightness temperature properties of a time dependent cloud radiation model, *J. Appl. Meteorol.*, *31*, 506–531.

Stein, J., E. Richard, J.-P. Lafore, J.-P. Pinty, N. Asencio, and S. Cosma (2000), High-resolution non-hydrostatic simulations of flash-flood episodes with grid-nesting and ice-phase parameterization, *Meteorol. Atmos. Phys.*, *72*, 203–221.

Tripoli, G. J., and W. R. Cotton (1982), The Colorado State University three-dimensional cloud/mesoscale model-1982. Part I: General theoretical framework and sensitivity experiments, *J. Rech. Atmos.*, *16*, 185–219.

Ulaby, F. T., R. K. Moore, and A. K. Fung (1986), *Microwave Remote Sensing*, vol. 3, *From Theory to Applications*, Artech House, Norwood, Mass.

Warren, S. G. (1984), Optical constants of ice from the ultraviolet to the microwave, *Appl. Opt.*, *23*, 1206–1225.

J.-P. Chaboureau, P. Mascart, O. Nuissier, and J.-P. Pinty, Laboratoire d'Aérologie, 14 avenue E. Belin, F-31400 Toulouse, France. (jean-pierre.chaboureau@aero.obs-mip.fr; masp@aero.obs-mip.fr; olivier.nuissier@aero.obs-mip.fr; pinjp@aero.obs-mip.fr)

J. R. Pardo, Departamento de Astrofísica Molecular e Infrarroja, Instituto de Estructura de la Materia, CSIC, Serrano 121, E-28006 Madrid, Spain. (pardo@isis.iem.csic.es)

C. Prigent, LERMA, Observatoire de Paris, 61 avenue de l'Observatoire, F-75014 Paris, France. (catherine.prigent@obspm.fr)

M. Wiedner, I. Physikalisches Institut, Universität zu Köln, Zülpicher Straße 77, D-50937 Köln, Germany. (wiedner@ph1.uni-koeln)